# Main Manuscript for

**Developmental progression of prefrontal circuit dysfunction in a Shank3$^{-/-}$ mouse model of autism spectrum disorder**

Gabrielle Devienne, Gil Vantomme, John R Huguenard*

Department of Neurology and Neurological Sciences, Stanford University, Stanford, CA, USA.

**Corresponding author:** John R Huguenard, Stanford Neuroscience Building S189, 290 Jane Stanford Way, Stanford, CA 94305-5088

**Email:** huguenard@stanford.edu

**Author Contributions:** Gabrielle Devienne: Conceptualization, Software, Formal analysis, Investigation, Writing - Original Draft, Visualization, Funding acquisition; Gil Vantomme: Software, Validation, Formal analysis, Investigation; John R Huguenard: Conceptualization, Software, Writing - Original Draft, Funding acquisition.

**Competing Interest Statement:** Authors have no conflict of interest to declare.

**Keywords:** prefrontal cortex, autism, electrophysiology.

**This PDF file includes:**

Main Text
Figures 1 to 7

**Abstract:**

Autism Spectrum Disorders (ASD) are a group of neurodevelopmental disorders with heterogeneous causes, characterized by communication deficits, impaired social interactions, and repetitive behaviors. Despite numerous studies focused on pathophysiological circuit mechanisms of ASD in mature mice, little is known regarding ASD onset and its evolution through development in these models. To explore early disruptions in mPFC development, we utilized the Shank3 knockout (Shank3$^{-/-}$) mouse model, a well-established genetic model of ASD. The medial prefrontal cortex (mPFC) is crucial for higher-order cognitive functions and social behavior, making it a key brain area of interest for understanding ASD pathology. SHANK3 is crucial for glutamatergic synapse maturation, and the Shank3$^{-/-}$ mouse has been well-characterized for displaying ASD-related behavioral phenotypes. We investigated network, cellular, and synaptic changes in the mPFC at two developmental stages, P14 and adulthood (>P55). Our findings revealed that while differences in neuronal excitability including hypofunction are detectable at P14, global mPFC dysfunction, including network hyperfunction and layer 5 pyramidal cell hyperexcitability, only becomes evident in adulthood. This suggests that early cellular changes that precede the development of behavioral deficits may lead to compensatory mechanisms that contribute to more pronounced mPFC deficits later in development. These results highlight the complex and evolving nature of mPFC dysfunction in ASD and suggest that early synaptic changes may set the stage for later behavioral and cognitive deficits.

**Introduction:**

Autism Spectrum Disorder (ASD) refers to a group of neurodevelopmental disorders characterized by communication deficits, impaired social interaction, and repetitive behaviors. ASD arises from complex etiologies including genetic causes and prenatal insults, making it difficult to precisely determine its onset. In humans, the behavioral deficits related to ASD are generally first observed in or after the second year of life[1,2], a period associated with rapid maturation of the medial prefrontal cortex (mPFC) [3], suggesting that abnormal maturation of this circuit may be in part responsible for ASD symptoms. In ASD genetic mouse models, communication deficits can be perceived in the early postnatal periods (pre-weaning; <P21)[4,5] , which corresponds to a critical period for both morphological and functional development of mPFC neuronal networks[6]. It is around the same period that mPFC develops long range connections with subcortical areas[6,7] including reciprocal connections with the mediodorsal thalamus[8]. Accumulating evidence implicates the role of mPFC in the regulation of social behavior[9–12]. The specific disruptions in mPFC development that contribute to ASD remain poorly understood. Identifying the specific changes that occur in the mPFC between early life and adulthood could reveal critical periods when the brain is most vulnerable to disruptions caused by ASD-related genetic mutations.

Genetic mutations may affect early brain development and/or mature function, thus, to identify early changes in mPFC we took advantage of the Shank3 complete knock out model (Shank3$^{-/-}$)[5]. SHANK3 proteins are involved in glutamatergic synapse maturation[13] and a loss of function of *Shank3* is a leading cause of ASD in humans[14,15]. Its corresponding Shank3$^{-/-}$ mouse model displays ASD-related phenotypes[5]. Interestingly, SHANK3 protein levels naturally decline around P14 during normal development[16], coinciding with a reduction in connectivity between the mPFC and its primary partner, the mediodorsal thalamus (MD)[17]. This provides a strong rationale for focusing on an early time point before mPFC - MD connections mature and then a later time point capturing the mature circuit.

In this study, we aim to investigate changes in mPFC from early life through adulthood using the SHANK3 KO model. By comparing network, cellular, and synaptic changes at P14 and adulthood (>P55), we aim to determine if disruptions in mPFC development begin early but remain subtle in infancy, only manifesting clearly later and contributing to the behavioral and cognitive deficits associated with ASD.

To address this question, we utilized behavior and different *in vitro* electrophysiological methods. Behavioral assessments confirmed social deficits in adult Shank3$^{-/-}$ mice and communication deficits

as early as P11, emphasizing the early onset of ASD-related symptoms in this model. Local field potential and whole cell patch-clamp recordings revealed that hyperactivity in the mPFC network emerges in adulthood, especially in deeper cortical layers, but is not present at P14. Hypofunction was observed in upper layers at P14. However, excitatory-inhibitory ratio alterations were already observable at P14 in Shank3$^{-/-}$ mice and persisted into adulthood, particularly in layer 5 cells. Layer 5 of mPFC contains subcortical projecting pyramidal cells that notably target the MD thalamus, and we tested whether this part of the circuit was disrupted. Repeated optogenetic activation of mPFC outputs resulted in persistent synaptic responses in MD cells with NMDAR and mGluR components that were augmented in Shank3$^{-/-}$ mice.

Altogether, these data indicate that mPFC deficits in Shank3$^{-/-}$ mice, such as network hyperfunction and layer 5 pyramidal cell abnormalities, become evident in adulthood, comparable to what is observed in other mouse models. This suggests that mPFC deficits may not be immediately apparent during early development, despite early signs of altered cell excitability and dendritic morphology. The mixed observations at P14 (hypoexcitability in layer 2/3 and signs of hyperexcitability in layer 5) may reflect an early stage of development that perhaps lays the groundwork for subsequent circuit reorganization. Or it may indicate that compensatory mechanisms balance each other out, masking any global changes in mPFC circuit function at this stage. However, our study demonstrates that more pronounced mPFC network deficits emerge later, potentially contributing to the different trajectories of communication and social behavior impairments observed in the progression of ASD. These novel findings highlight that even though mPFC network deficits and affected behavior become more severe later in development, early synaptic changes are already present in early stages, potentially setting up the network for future alterations. Our results demonstrate a progressing dynamic of mPFC deficits in ASD which raises the possibility that early manipulation could prevent some of the related behavioral deficits observed later.

## Results:

### Early emergence of social behavioral deficits in Shank3$^{-/-}$ mice.

To assess the development of potential behavioral deficits in the Shank3 complete knockout (Shank3$^{-/-}$) mouse model, we conducted behavioral tests at two distinct developmental stages: pups (P11) and adults (>P55). Given the limited mobility of pre-weaning mouse pups, evaluation of ultrasonic vocalization (USV) can be used as a proxy of social behavior[18]. Shank3$^{-/-}$ P11 pups produced many fewer calls when isolated compared to their wild type (WT) littermates (Figure 1 A-C; mean ± sem; WT: 253 ± 58.1 calls; Shank3$^{-/-}$: 60.8 ± 30.4 calls; testing period 8 minutes; Mann-Whitney, p=0.01). Consistent with a further social deficit that persists into adulthood, mature Shank3$^{-/-}$ mice failed to show a social preference in the three chamber interaction test, showing similar times with either a novel inanimate object or a novel conspecific mouse, in contrast with adult WT mice, which showed a social preference (Figure 1 D-F; interaction time, mean ± sem; WT: mouse, 33.1 ± 4.95, object, 15.8 ± 1.95 %, paired t-test, p= 0.02; Shank3$^{-/-}$: mouse, 14.6 ± 5.62, object: 15.8 ± 5.91%, paired t-test, p= 0.89). These results align with previous literature on ASD mouse models[19–21], including the complete Shank3 knockout[5]. We therefore confirm that behavioral deficits begin as early as P11, which correlates with crucial development in the circuit connections between the medial prefrontal cortex (mPFC) and mediodorsal thalamus (MD) [6,8], an important circuit related to social behavior[22].

### Shift in developmental mPFC network activity toward hyperfunction.

To investigate potential mPFC developmental dysfunction, we employed an *in vitro* network excitability approach. We obtained coronal brain slices containing the mPFC from Shank3$^{-/-}$ mice and WT littermates at different developmental stages, including P11, P14, and adulthood (refer to Figure 2 and Supplementary Figure 1). Using a 16-shank linear silicon probe array positioned across the layers of the mPFC, we recorded network activity in the form of local-field potentials (LFPs). Local electrical stimulation of deep layers evoked LFPs that could be observed across all cortical layers, indicating engagement of intra-cortical circuits (Figure 2A). To localize the LFP signals to different cortical layers, we calculated the current source density (CSD) as the second spatial derivative of the LFP (Figure 2B

and C[23]). This allowed us to compare network differences between Shank3$^{-/-}$ mice and WT littermates. We observed matched pairs of sinks and sources in the CSD profiles following local electrical stimulation in the deep layers. Sinks are negative CSD signals generally attributed to the movement of cations from the extracellular space into the cells during synaptic excitation. Given conservation of charge, such ionic current flow must be matched with a paired outward flow of cations (sources) from these cells at a distance from the original sinks. Synaptic inhibition has the opposite polarity of sinks/sources as it is mainly associated with anionic current flow. Accordingly, sources/sinks cannot unambiguously be associated with either excitation or inhibition. However given that the majority of synapses in neocortical circuits are excitatory[24–26], sinks will be dominated by direct excitatory signals, and sources with their return path. We applied a subtractive pharmacological approach to isolate components of CSD signal, to reveal distinct pre- and post-synaptic components, with the post-synaptic components being blocked by DNQX and CPP, AMPA and NMDA receptor antagonists, as illustrated in Supplementary Figure 1B.

We initially assessed mPFC excitability at the two stages that we had previously characterized behaviorally, P11 and adult. At P11 we observed LFP and CSD components generally comparable to what was observed in adult mice, although with somewhat simpler features, consistent with the immature state of the network at P11 (Figure 2A, vs. Supplementary. Figure 1C). We did not detect any differences between Shank3$^{-/-}$ mice and their WT littermates at P11. We then selected P14 as the next developmental time point. This choice corresponds to a developmental stage marked by significant changes in SHANK3 protein levels[16]. The CSD signal at P14 showed sinks and sources across layers that were more complex than at P11, and more similar to the CSD responses in adults. At P14, slices from Shank3$^{-/-}$ mice did not show differences from WT littermates in any of the major CSD components we identified, either the layer 2/3 presynaptic sink, the postsynaptic layer 2/3 source or the layer 5 postsynaptic sink. By contrast, mPFC slices from adults demonstrated hyperexcitability in Shank3$^{-/-}$ mice (Figure 2B-D). Closer inspection revealed that this overall increase in CSD signal is mediated by an increase in the peak amplitude of the layer 2/3 presynaptic sink and the postsynaptic layer 5 sink (Figure 2CD Adults; 2-way ANOVA with repeated measure, layer 2/3 presynaptic sink: genotype $p=0.004$, stimulation $p<0.0001$, interaction $p<0.0001$; layer 5 postsynaptic sink: genotype $p=0.01$, stimulation $p<0.0001$, interaction $p=0.04$). There is also a trend for an increase in the peak amplitude of layer 2/3 postsynaptic source in adult Shank3$^{-/-}$ mice (Figure 2D Adults; 2-way ANOVA with repeated measure, layer 2/3 postsynaptic source: genotype $p=0.051$, stimulation $p<0.0001$, interaction $p=0.08$). Altogether, these data show the emergence of a hyperfunctional mPFC network between P14 and adulthood (>P55) in the Shank3$^{-/-}$ mouse model.

**Developmental emergence of hyperexcitability of layer 5 mPFC pyramidal cells.**

Our *in vitro* LFP experiments revealed increased mPFC network activity in Shank3$^{-/-}$ adult mice, evidenced in both presynaptic and postsynaptic signals. These results suggest potential alterations in the properties of local mPFC cells or in the synaptic inputs to the mPFC. Excitatory pyramidal neurons in the mPFC are crucial for regulating cognitive and social behavior[27]. Layer 2/3 of the mPFC receives diverse long-range inputs, including notable projections from the MD thalamus[28]. Conversely, layer 5 of the mPFC primarily projects to the MD thalamus, although not exclusively [6,29,30] as it can target other subcortical areas but also the contralateral hemisphere of the mPFC.

To investigate changes in cellular excitability, mPFC layer 2/3 and layer 5 pyramidal cells were recorded at P14 and in adults (>P55). Early in development L2/3 pyramidal cells revealed hypoexcitability with a hyperpolarized resting membrane potential (Figure 3A; RMP, P14; mean ± sem; WT: -58.6 ± 1.25 vs Shank3$^{-/-}$: -62.8 ± 1.28; $p=0.03$, Welsh t-test) which is not observed in adults. In addition, we found that Shank3$^{-/-}$ P14 pyramidal cells fired significantly fewer action potentials in response to depolarizing current steps (Figure 3B; 2-way ANOVA; genotype $p=0.0002$, current injection $p<0.0001$, interaction $p<0.0001$). In contrast, in adulthood this hypoexcitability was no longer evident in layer 2/3 cells (Figure 3C).

Various ASD mouse models have been shown to display hyperexcitability of adult mPFC layer 5 pyramidal cells[12,31,32]. Consistent with this, we find that layer 5 Shank3$^{-/-}$ pyramidal cells have a depolarized RMP (Figure 3D; RMP; Adults; mean ± sem; WT: -67 ± 1.3 vs Shank3$^{-/-}$: -63.4 ± 1.2, p=0.048, Welsh t-test). Similar results were observed at P14 (Figure 3D; RMP; P14; mean ± sem; WT: -63,0 ± 1.3 vs Shank3$^{-/-}$: -57,4 ± 1.4, p=0,005, Welsh t-test). This early sign of hyperexcitability is also reflected by a higher input resistance (Figure 3D; RMP; P14; mean ± sem; WT: 304 ± 29.1 vs Shank3$^{-/-}$: 448 ± 33.7, p=0.003, Welsh t-test). At P14, layer 5 pyramidal cells display a similar number of action potentials in response to depolarizing current injection in Shank3$^{-/-}$ and WT littermates (Figure 3E). Interestingly, Shank3$^{-/-}$ adult layer 5 pyramidal cells display higher number of action potentials in response to depolarizing current injection (Figure 3F; 2-way ANOVA; genotype p= 0.0058, current injection p<0.0001, interaction p<0.0001). In addition, Shank3$^{-/-}$ adult layer 5 pyramidal cells also display an increased value of Sag+Rebound compared to their WT littermates (Supplementary Figure 2 B5, p=0.04, Welsh t-test). We did not observe any rheobase action potential properties alterations at both age and in both layers (Supplementary Figure 2).

In summary, our whole-cell patch-clamp recordings revealed signs of hypoexcitability in mPFC layer 2/3 pyramidal neurons in juvenile but not adults Interestingly, we revealed early signs of hyperexcitability in juvenile Shank3$^{-/-}$ layer 5 pyramidal cells which persist with greater functional consequences in adults.

**Morphological differences mPFC layer 5 pyramidal neurons of Shank3$^{-/-}$ mice**

Biocytin was included in our intracellular recording solution, which allowed us to label a subset of mPFC layer 5 pyramidal cells in both WT and Shank3$^{-/-}$ at P14 and in adults. A Scholl analysis at both ages revealed an increase in dendritic complexity in Shank3$^{-/-}$ cells (Figure 4B; 2-way ANOVA, P14, genotype p=<0.0001, distance p=<0.0001, interaction p=<0.0001; Adults, genotype p=<0.0001, distance p=<0.0001, interaction p=<0.0001). Layer 5 pyramidal neurons from Shank3$^{-/-}$ mice showed an increase in the number of arborizations close to the soma (Figure 4A-B). This observation is supported by an increased number of branches in Shank3$^{-/-}$ mice (Supplementary Figure 4A1). In addition, adult Shank3$^{-/-}$ mice neurons have more branching points compared to WT mice (Supplementary Figure 4B1). The average length of individual neurites is similar between WT and Shank3$^{-/-}$ mice. It has been described that layer 5 pyramidal cells can be split in at least two different subtypes: subcortically projecting, thick-tufted neurons that display a marked H-current, and callosal projecting, thin-tufted neurons that display an absence in H-current[33,34]. To exclude the possibility that these findings represent differences in the proportions of recorded cell subtypes in Shank3$^{-/-}$ vs WT animals, we measured apical dendritic shaft width in WT and Shank3$^{-/-}$, which did not show any significant differences (Supplementary Figure 4D) suggesting that our morphological analysis was performed in comparable mPFC neuron populations. Furthermore, we measured the hyperpolarization induced membrane potential sag, reflecting activation of h-current[35,36], and did not observe differences between WT and Shank3$^{-/-}$ mice. This result also suggests that the recorded populations of layer 5 subtypes in our recording sample were similar between WT and Shank3$^{-/-}$ mice. Overall, WT/ Shank3$^{-/-}$ mPFC layer 5 pyramidal neuron increases in excitability and dendritic complexity are already present at P14 and persist into adulthood.

**Decreased E-I ratio observed at P14 and in the adult Shank3$^{-/-}$ mice**

A major goal in ASD research has been to find convergent mechanisms in different genetic mouse models. One of the main hypotheses proposed by Rubenstein and Merzenich[37] is linking genetic models of autism to a common cortical increase in excitatory-inhibitory ratio. We used whole-cell voltage-clamp recordings to examine the synaptic responses in mPFC layer 2/3 and layer 5 pyramidal cells. Excitatory postsynaptic currents (EPSCs) recorded at -70mV and inhibitory postsynaptic currents (IPSCs) at +10mV were evoked using an electrical bipolar stimulating electrode placed in upper layer 2/3 (Figure 4A). mPFC layer 2/3 pyramidal cells did not show Shank3$^{-/-}$ related excitatory-inhibitory ratio imbalance at either P14 or in adults (Supplementary Figure 3B). By contrast, mPFC layer 5 pyramidal cells displayed a reduced E-I ratio at P14 (Figure 4B-C; mean ± sem; P14 WT: 0.98 ±0.21, P14 Shank3$^{-/-}$:

221 0.4 ± 0.1, Mann Whitney test, p=0.04) that continued into adulthood (Figure 4B-C; mean ± sem; WT: 1.0
222 ± 0.3, Shank3$^{-/-}$: 0.55 ± 0.1, Mann Whitney test, p=0.047). These data, in contrast to previous
223 observations made in other ASD models, suggest that the imbalance of the E-I conductance ratio in
224 Shank3$^{-/-}$ mice shows a decrease and is restricted to layer 5 of the mPFC. Interestingly, this imbalance
225 is observed as early as P14, indicating that these alterations in synaptic function occur during early
226 developmental stages, potentially contributing to the onset and progression of ASD in Shank3$^{-/-}$ mice.

227 **Altered mPFC- MD thalamus synaptic function in Shank3$^{-/-}$ mice.**

228 As outlined above, one of the major projections of mPFC layer 5 pyramidal cells is the MD thalamus. To
229 evaluate whether the changes we observed in mPFC were associated with and potentially causative of
230 effects on downstream targets, we injected mPFC with a Channelrhodpsin2 expressing virus (AAV1-
231 CaMKIIa-ChR2-eYFP) and following in vivo incubation for several weeks, we recorded responses in MD
232 cells (Figure 6A). Shank3$^{-/-}$ MD neurons showed passive properties that were indistinguishable from
233 controls (Supplementary Figure 5A1-4), indicating that the previous changes in excitability we observed
234 were restricted to cortical locations. Using 1Hz blue light stimulation, we reliably evoked optogenetically
235 induced Shank3$^{-/-}$ monosynaptic excitatory synaptic currents (oEPSCs) as observed with a short
236 latency (in ms; mean ± sem; WT=2.6 ± 0.1; Shank3$^{-/-}$ = 2.9 ± 0.1; p=0.1). oEPSCs showed similar
237 latency and rise time between WT and Shank3$^{-/-}$ (in ms; mean ± sem; WT= 2.2 ± 0.1; Shank3$^{-/-}$ = 2.1
238 ± 0.1; Mann Whitney test, p=0.7) but different decay time (WT= 22 ± 11.5; Shank3$^{-/-}$ = 30.2 ± 19, Mann
239 Whitney test, p=0.03) (Figure 6B). Thus, mPFC stimulation generates longer lasting oEPSCs resulting
240 in a greater synaptic charge to MD in Shank3$^{-/-}$. The peak evoked synaptic current amplitudes did not
241 differ between WT and Shank3$^{-/-}$ mice (Supplementary Figure 5B1-2), indicating that the observed
242 differences in EPSC decay rate were not due to differences in viral efficiency or spread. We noticed that
243 during 10 Hz trains, the synaptic current did not fully decay to baseline between individual responses of
244 the train (Figure 6C). We term this build-up the persistent part of the synaptic response, which
245 accumulates over the course of the oEPSC train. We classified MD neurons based on the amplitude of
246 the persistent current at the end of the train of stimulation (end of oEPSC #9, Figure 6C1). In WT mice,
247 about 2/3 of MD cells 22/34 showed a persistent current at the end of the train of stimulation of at least
248 10 pA. By contrast, in Shank3$^{-/-}$ mice most MD cells exhibit a persistent current (28/32 cells, Figure 6C2,
249 chi-square test, p=0.03). Thus, our results demonstrated a significant difference in the proportion of MD
250 cells showing a late synaptic response between WT and Shank3$^{-/-}$ mice. Similarly, the buildup of
251 persistent current across the 10 stimulations at 10 Hz is greater in Shank3$^{-/-}$ than in WT (Figure 6 C4,
252 WT vs Shank3$^{-/-}$, 2-way ANOVA with repeated measure, genotype p=0.02, stimulation p=<0.0001,
253 interaction p=<0.0001).

254 We found that upon termination of oEPSC trains MD neurons displayed a slowly-decaying "late
255 persistent" response lasting for several seconds. We measured this as the current 500ms following the
256 end of the stimulus train and found that the late persistent current was greater in Shank3$^{-/-}$ mice (Figure
257 6C1 and C5; mean ± sem; WT = -12.2 ± 3.2; Shank3$^{-/-}$ = -22.8 ± 4.1, Mann-Whitney test, p=0.002).
258 These findings indicate increases in the connection strength between mPFC and MD neurons in
259 Shank3$^{-/-}$ mice. This strengthening becomes especially evident during 10 Hz stimulus trains and leads
260 to greater recruitment of MD cells as measured by numbers of evoked action potentials (Figure 6D1-2,
261 WT vs Shank3$^{-/-}$, 2-way ANOVA with repeated measure, genotype p=0.049, stimulation p=<0.0001,
262 interaction p=0.0001).

263 **Synaptic receptors underlying the augmented function of the mPFC-MD synapse**

264 To investigate the nature of the large persistent current in Shank3$^{-/-}$ mice, we conducted a set of two
265 separate experiments using pharmacological compounds targeting two major receptor classes known
266 to be affected by Shank3 mutations in other brain regions. Additionally, we chose to target receptors
267 with a long duration of action, based on the previously observed increase in oEPSC decay time and the
268 presence of late persistent current in Shank3$^{-/-}$ mice (Figure 6). First, we used AP5, an antagonist of
269 NMDA receptors. Second, we conducted an occlusion experiment using DHPG, which is an agonist of

mGluR1 and mGluR5 receptors. These drugs were applied only if the recorded cell exhibited at least 10 pA of persistent current. We found that application of either AP5 at 0.1μM (Figure 7A-C) or DHPG at 10μM (Figure 7D-F) decreased the phasic current in Shank3$^{-/-}$ mice (2 way-repeated ANOVA, bath vs AP5, drug p=0.009, stimulation p=0.3, interaction p=0.9; bath vs DHPG, drug p=0.003, stimulation p=0.7, interaction p=<0.0001) but not in WT mice (Figure 7A,B,D,E; 2 way-repeated ANOVA; bath vs AP5, drug p=0.9, stimulation p=0.099, interaction p=0.0002; bath vs DHPG, drug p=0.08, stimulation p=0.3, interaction p=<0.0001). Moreover, pharmacology targeting NMDAR or mGluR1 and 5 had no effect on the persistent current in WT mice but decreased it in Shank3$^{-/-}$ mice (interaction p=0.9; bath vs DHPG, drug p=0.003, stimulation p=0.7, interaction p=<0.0001) but not in WT mice (Figure 7A,C,D,F; 2 way-repeated ANOVA; bath vs AP5, drug p= 0.0001, stimulation p<0.0001, interaction p <0,0001; bath vs DHPG, drug p= 0,0016, stimulation p=<0.0001, interaction p=<0.0001).

## Discussion

In this study, we investigated the atypical development of the medial prefrontal cortex (mPFC) using the Shank3$^{-/-}$ mouse model of autism spectrum disorder (ASD). After initially assessing function at P11, we mainly compared relevant developmental time points, specifically P14 (pre-weaning stage) and adulthood (>P55). Initially, we confirmed known ASD-related behavioral deficits, including impaired social behaviors in adult mice and altered ultrasonic vocalizations (USVs) in juvenile mice. We then employed our in vitro local field potential (LFP) recording design, which allowed us to identify a significant difference between the P14 and adult stages, revealing that mPFC circuit hyperfunction is observable only in adults. Furthermore, using whole-cell patch-clamp recordings of pyramidal cells, we uncovered distinct developmental patterns between cortical layers: at P14, layer 2/3 pyramidal cells exhibited hypoexcitability, while layer 5 cells showed signs of hyperexcitability. As the mice matured, the hyperexcitability in layer 5 cells was exacerbated, whereas layer 2/3 cells tended to normalize their excitability. Interestingly, we observed that the excitation/inhibition (E/I) ratio was altered specifically in layer 5 neurons at both developmental stages, while no significant changes were observed in layer 2/3 cells. These findings led us to further investigate the mPFC-mediodorsal (MD) thalamus pathway, a major connection involved in social behavior. We observed significant alterations in this pathway, with changes in synaptic strength and post-synaptic receptor composition in Shank3$^{-/-}$ mice, which were linked to disruptions in NMDA and mGluR group 1 receptor signaling.

### Longitudinal approaches in ASD research

While much of the research on autism spectrum disorder (ASD) focuses on neurodevelopmental mechanisms such as circuit activity, synaptic connections, and neuronal physiology in mature animals, there is a growing interest in longitudinal studies. The development of genetic mouse models of ASD offers the opportunity to investigate the effects of specific gene mutations across multiple scales, e.g., behavioral, circuit-level, and molecular, throughout the lifespan. Our study has confirmed that some behavioral alterations appear in Shank3$^{-/-}$ as young as P11. Additionally, at the single-cell level, we observed that layer 2/3 pyramidal cells in the mPFC are hypoexcitable in early development, while those in layer 5 exhibit signs of hyperexcitability. Layer 5 cells also displayed altered morphology. Similar observations of early cellular deficits have been reported in other studies using a different Shank3 mutant model, Shank3B$^{-/-}$,in the corticostriatal circuit, where abnormal hyperactivity of corticostriatal afferents was observed[38]. This group also confirmed early behavioral alterations in the Shank3B$^{-/-}$ model[39]. Altered USVs are also commonly observed in various genetic mouse models of ASD[4]. These observations suggest that longitudinal approaches, such as our work, can provide critical insights into how gene mutations influence the progression of ASD over time and might help reveal potential targets and windows for therapeutic intervention.

### mPFC Layer-Specific Excitability in ASD

As mentioned above our study has found mPFC layer specific deficits that are different at P14 compared to the adults. The scientific literature regarding mPFC dysfunction has largely focused on mature animals[12,20,40,41]. The hyperexcitability results of mPFC layer 5 pyramidal cells is consistent with

observation made in other mouse model[12,32,42]. However, other reports suggest that mPFC layer 2/3 cells are altered[27,41]. Our results introduce a novel finding, where we observed changes in mPFC pyramidal cell excitability depending on the animal age. Specifically, we detected hypoexcitability in layer 2/3 cells at P14, while layer 5 cells exhibited only a mild hyperexcitability - depolarized resting membrane potential - at this stage. We can speculate that compensatory mechanisms may normalize layer 2/3 cell excitability by adulthood, while at the same time it could indirectly lead to hyperexcitability in layer 5 cells in adult mice. Pyramidal cell morphology and intrinsic membrane properties develop in parallel in layers 2/3 and 5. However, the development of synaptic inputs differs between these layers[43] : during the first two postnatal weeks, layer 2/3 primarily receives excitatory inputs, while layer 5 does not[44]. Shank3 is a scaffolding protein found in excitatory synapses[45,46]. Its knockout may first affect early-developing synapses in layer 2/3 before impacting those in layer 5. This suggests that different layers of the mPFC may be affected differently to different ASD- related gene mutations. It also highlights the heterogeneity of ASD-related neurodevelopmental changes, where distinct mPFC layers might display alterations at different developmental stages. Consequently, these findings underscore the importance of considering both layer-specific and age-dependent parameters when studying pathophysiological mechanisms linking to ASD.

**E/I ratio theory in ASD**

Twenty years ago, Rubenstein and Merzenich hypothesized that ASD dysfunction may generally be related to increase in excitatory/ inhibitory ratio[37]. This theory has been of interest of many[10,47] as it can relate to different ASD mouse models. Recently, Antoine et al. [48] has observed an elevated E-I ratio is a common circuit phenotype in four different genetic mouse models of ASD. They demonstrated that this elevation reflects stabilization of synaptic drive rather than driving network hyperexcitability, as was previously believed. Surprisingly, in our study, we observed a reduction in the E/I ratio in Shank3$^{-/-}$ mPFC layer 5 cells at both P14 and in adults. Yet LFP recordings demonstrated global mPFC hyperfunction and layer 5 pyramidal neuron hyperexcitability in adults, but less at P14. These results align with the findings of Antoine et al. and challenge the previous theory that hyperexcitability is the primary cause.

**mPFC- MD synaptic connectivity**

Adult Shank3$^{-/-}$ mice exhibit altered mPFC-MD thalamus synaptic connectivity which results in a functional increase in mPFC-driven MD neuron spikes. In addition, we also observed a greater incidence of persistent synaptic responses in MD neurons of Shank3$^{-/-}$ mice that might be related to behavioral dysfunction. In agreement with our observation of altered corticothalamic connectivity, it has been shown that sensory cortico-thalamic synapses are also altered in adults Shank3$^{-/-}$ mice[49]. Clues for a critical period of development for the mPFC-MD circuit have emerged. Indeed, anatomical lesions[50] or chemogenetic modulation to disturb the mPFC-MD circuit before adulthood results in physiological changes of mPFC activity[51,52] or social behavior[51]. Similar modulation in adulthood failed to affect mPFC circuits or social behavioral changes. It is interesting to note that the density of connections between the mPFC and MD regions decreases at postnatal day 14 (P14)[6] and that a similar decrease in the expression of the SHANK3 transcript occurs at the same time point[16]. Overall, it highlights the critical role of the mPFC-MD thalamus circuit in adult Shank3$^{-/-}$ mice, demonstrating that alterations in this circuit are evident in adulthood and emphasizing the need to understand how early developmental changes contribute to these persistent adult alterations.

**Caveats and future directions**

Here we demonstrated novel findings of developmental ASD-related circuit dysfunction in a model of severe ASD, Shank3$^{-/-}$ mice, at two important time points: P14 and adults (>P55). However, a potential limitation of our results is that they were mainly obtained in isolated brain slices. These have the advantage of being accessible for mechanistic and pharmacological characterization, using LFP or cellular physiology. However, the conditions *in vitro* can never match those in the intact brain, and any disease-related differences in extrinsic connectivity, neuromodulatory state, etc. will not be directly

revealed by the in vitro approach. Yet, the use of optogenetics and pharmacology has the advantage of better understanding of pathophysiological mechanisms directly related to genetic mutations. One potential drawback of LFP network analysis is that the electrical synaptic stimulation approach involves a single extracellular stimulus pulse that evokes a simplified and highly synchronized input that may not model normal ongoing circuit activity in behaving animals. Yet, being able to reliably and quantitatively determine input-output relationships provides an integrated assay of circuit excitability, and potentially E/I ratio, that outweighs this limitation. Further, given that both WT and Shank3$^{-/-}$ slices received comparable stimulation, yet displayed different responses, with hyperfunction of mPFC observed in adult Shank3$^{-/-}$, it indicates that the circuit state in Shank3$^{-/-}$ is more sensitive to synaptic input than in the WT. It would be interesting in the future to perform similar experiments *in vivo* by for example optogenetically stimulating the MD thalamus axon in mPFC while recording mPFC activity with linear silicon multielectrode probes. Another limitation of our study is that as of now, there is no direct evidence of a link between early circuit dysfunction and later behavioral effects. Using in vivo recording, like fiberphotometry[53] or miniscope[22] during the social interaction task will allow to relate the activity of mPFC (bulk fiberphotometry signal) or mPFC cells (miniscope) to the deficits. Finally, our study can be a starting point for establishing a causal link between early neurodevelopmental events and ASD-relevant neural circuit alterations. Acute mPFC circuit manipulation using optogenetics[53] or chemogenetics[51,54] in the adults have been shown to be able to rescue some social behavior. It will be interesting to see if similar manipulations performed chronically during early life will have a significant impact on adult physiology and behavior. By identifying these critical periods of mPFC development, we might be able to perform early interventions that may prevent or mitigate ASD-related circuit dysfunction.

## Materials and Methods

### Animals

The mice were bred and maintained according to Stanford University, School of Medicine Animal Research Requirements, and all procedures were approved by the Committees on Animal Research at Stanford University (protocol number: 12363). Mice carrying the *Shank3* complete knock out (Δe4–22) were a kind gift from Dr. Yong-Hui Jiang[5], Duke University. All comparisons were made using both genders. Mice used for experiments were separated in two distinct age group: P14 (+/- ½ day) and adults (2-4 months). The mice were maintained on a 12 hr light/dark cycle. Food and water were available ad libitum.

### Genotyping of transgenic animals

Shank3$^{-/-}$ and Shank3 WT mice were genotyped by PCR using the following primers: wild-type forward GTGCCACGATCTTCCTCTAAAC, wild-type reverse, AGCTGGAGCGAGATAAGTATGC, mutant forward TTGCATCTGGGACCTACTCC and mutant reverse AAAGCACTGACTCCTCTCTTGG.

### Behavioral tests

*Ultrasonic vocalization recordings*

Ultrasonic vocalizations are typically emitted by pups from birth to the weaning period and are related to communication behavior. In this study, we used an isolation protocol-based test to elicit ultrasonic vocalizations (USVs) by isolating the pups briefly from their dams and littermates[55]. Specifically, one hour before the recordings, on postnatal day 11 (P11) the breeders were removed from the house cage. The house cage with the remaining litter was then moved to the testing room and placed on a heating pad for one hour to maintain the body temperature. Pups were then individually isolated. Each tested pup was placed in a testing cage within a sound-isolated, dark box, with an UltraSoundGate 116Unb recording system (Avisoft Bioacoustics) positioned 15 to 20 cm above. The USV were recorded with a sampling rate of 384,000 Hz in a 16-bit format (recording range: 0-250 kHz) for 10 minutes using the Avisoft-RECORDER USG/USGH software (Avisoft Bioacoutisc). Finally, the pup was returned to its home cage with its littermates. Once the entire litter had been tested, the home cage was returned to its original room, and the breeders were placed back in the cage. The recordings were next analyzed using the Avisoft-SASLab Pro software (version 5.3.2-14; Avisoft Bioacoustics). In recordings of pup

vocalizations over a 10-minute period, the first 2 minutes are excluded from analysis as the calls may result from handling-related stress. Fourier transformation (512pt FFT, Frame=100%, Hamming window with 75% of time overlap) was applied to obtain the spectrograms (500Hz: Frequency resolution; 0.5ms: Time resolution). USV detection was performed using automatic whistle tracking. Monotonic calls with a minimal duration of 5 ms and slope of -15 to 6kHz/ms were counted. Number of calls was tested for Normality using a Shapiro-Wilk test. Between-group comparison was performed using a non-parametric Mann Whitney test. Data are reported as mean+/- sem.

*Social preference test*

To measure sociability, mice were tested in a social interaction task. For this test, a clean box was partitioned into three zones. A camera was mounted directly above the box to record videos that were analyzed offline. Tested mice were habituated to the empty box for ten minutes, the first day. The next day, a pre-test phase was performed using two empty cages on each side of the box. The tested mouse had 10 minutes to explore. The test phase is performed 10 minutes later. A novel object was placed in a cage at one side of the box and a conspecific is placed in a cage at the opposite side of the box. The placement side for the novel object and never-met mouse was randomly assigned. Using EzTrack[56] , the videos were scored to determine the time the tested mouse spent in regions of interest (ROIs) drawn around the cage containing either the novel object or the conspecific. After checking for normality, the interaction time between an inanimate object or conspecific was tested using a Welch's t-test.

**Extracellular multielectrode recordings**

Extracellular recordings were performed on neocortical coronal 400 µm thick slices from P14 or adults (>P60) Shank3$^{-/-}$ (KO) or Shank3 wild type (WT) containing the medial prefrontal cortex (mPFC). Slices were recorded in a humidified oxygenated interface chamber at 34°C and perfused at a rate of 2 ml/min with oxygenated artificial cerebrospinal fluid (aCSF). The aCSF contained (in mM): 10 glucose, 26 $NaHCO_3$, 2.5 KCl, 1.25 $NaHPO_4$, 1 $MgSO_4$, 2 $CaCl_2$, and 126 NaCl (300 mOsm).
A linear silicon multichannel probe (16 channels, 100 µm inter-electrode spacing, NeuroNexus Technologies) was positioned throughout all layers of the mPFC to record evoked local field potentials (LFPs). The silicon probe was linked to a pre-amplifier (PZ5-32, Tucker-Davis Technologies (TDT)), and recordings were made using an RZ5D processor (TDT). Data acquisition was conducted using the Real-time Processor Visual Design Studio (RPvdsEx) tool and a custom Python code. LFP data were acquired at 25 kHz and filtered between 0.1 and 500 Hz. A bipolar tungsten microelectrode (each wire, 50-100 kΩ, FHC) positioned in upper layer 5 was used to deliver a bipolar electrical stimulation (0.1ms duration, intensity loops from 100 to 800 µA, interval of 15s). To obtain a more reliable index of the location, direction, and magnitude of currents underlying synchronous network activity, we derived the current-source density (CSD) from raw LFP signals[23]. Assuming a uniform extracellular resistivity, the CSD can be estimated as it is the second spatial derivative of the LFP. In our experiment, CSD was computed in mPFC by algebraic differentiation of the LFP at adjacent electrodes in the linear probe spaced by 100µm and assumed a uniform extracellular resistivity of 0.3 S/m[57]. In addition, the following drugs, DNQX (AMPAR antagonist; 25uM) and CPPene (SDZ EAA 494; NMDA competitive antagonist; 1µM) were applied in the bath to identify the pre and post synaptic component of our signals. Relevant components were next identified based on their distinct shape and their amplitude was measured for each slice. Between-group comparison was performed using a 2-way repeated measure ANOVA. Data are reported as mean+/- sem.

**Electrophysiological whole-cell patch-clamp recordings in mPFC slices**

Mice were deeply anesthetized with isoflurane (for P14 mice) or pentobarbital sodium (i.p., 50mg/kg; for adult mice). P14 mice were directly decapitated. Adult mice were perfused transcardially with ice-cold (4ºC), oxygenated (95% $O_2$ /5% $CO_2$) sucrose slicing solution containing (in mM): 234 sucrose, 11 glucose, 26 $NaHCO_3$, 2.5 KCl, 1.25 $NaH_2PO_4$, 10 $MgSO_4$, and 0.5 $CaCl_2$ (310 mOsm). Brains were quickly removed and 250 µm-thick coronal slices of mPFC cortex were cut in sucrose ACSF using a vibratome (VT1200; Leica). Slices were transferred to a holding chamber filled with standard ACSF bubbled with 95% $O_2$ and 5% $CO_2$. The composition of aCSF was (in mM): 10 glucose, 26 $NaHCO_3$, 2.5 KCl, 1.25 $NaHPO_4$, 1 $MgSO_4$, 2 $CaCl_2$, and 126 NaCl (300 mOsm). Slices were allowed to recover 30 minutes at 37°C and were then incubated at room temperature (20–25°C) until recording.

Individual slices were transferred to a recording chamber and continuously perfused at 2ml/min with oxygenated aCSF at room temperature. Patch pipettes (3-5 MΩ) were pulled from borosilicate glass (Sutter Instrument, CA, USA) on a micropipette puller (Model P1000, Sutter Instrument, CA, USA) and filled with an intracellular solution containing (in mM): K-gluconate, 144; $MgCl_2$, 3; HEPES, 10; EGTA, 0.5 and 2 mg/ml biocytin, pH= 7.2, 270mOsm (that's low. The one we prepared were 290). Whole-cell patch-clamp recordings were obtained from layer 2/3 or layer 5 pyramidal cells selected based on their morphology and electrophysiological profile. Recordings were performed at room temperature (20–25°C) using a patch-clamp amplifier (Multiclamp 700B, Molecular Devices) connected to a Digidata 1440A interface board (Molecular Devices). Signals were amplified and collected using the data acquisition software pClamp 10.7. Resting membrane potential was measured just after passing into whole-cell configuration, and only cells with a resting membrane potential more hyperpolarized than −50 mV were selected. Resting membrane potential was computed as the average of the sweeps were no current was injected. Membrane potentials were not corrected for junction potential. Cells were held at their resting membrane potential and V/I curves were constructed from a series of current steps in 10pA and 20pA increments. Input resistance was determined from the slope of the V/I curve near resting membrane potential. Rheobase was calculated as the minimal depolarizing current step triggering an action potential. A tungsten bipolar stimulating electrode was placed in mPFC layer 2-3 to evoke at -70mV excitatory current and using the same intensity at +10 mV an inhibitory current. The peak amplitude of these excitatory and inhibitory evoked responses was used to calculate the excitatory-inhibitory ratio. Results are given as mean ± standard error of the mean (sem). Between-group comparisons were performed using parametric test. A p-value below 0.05 was considered statistically significant.

After recordings, slices were fixed overnight at 4°C in 4% paraformaldehyde/ PBS and then washed in PBS. Slices were processed using Alexafluor 488-conjugated streptavidin (1:500, Invitrogen) to reveal biocytin. After a series of wash in PBS, slices were mounted on gelatin-coated slides in Fluoromount-G for confocal microscopy.

**Morphological analysis**

Zeiss LSM900 laser scanning confocal microscope was used to image the mPFC layer 5 biocytin labelled neurons with 63x objectives and a 488nm laser. Images were processed using ImageJ (National Institutes of Health; http://rsbweb.nih.gov/ij/). Neuronal tracing and analysis were performed using the SNT toolbox[58].

**Viral injections**

For adult experiments, the procedure for viral injection has been described in detail in[59]. Briefly, young adult mice were anesthetized using isoflurane (3% induction, 1.5% maintenance) and received carprofen 5 mg/kg intra peritoneal injection. Mice received bilateral injection in mPFC (in mm from bregma, AP 1.8, ML 0.5, DV -2.6). A volume of 500nl of virus encoding the ChR2 (AAV1-CaMKIIa-ChR2(H134R)_eYFP-WPRE-HGH, $10^{12}$ GC, 100 nl/min, Penn Vector Core, Addgene 26969P) was delivered to the injection sites.

For P14 experiments, P0 mice were anesthetized on ice. Mice received a bilateral injection in the frontal area (in mm from lambda, AP: 3.5, ML:0.1, DV:1.5). A volume from 100 to 200nl of virus encoding the ChR2 (AAVDJ-CaMKIIa-ChR2(H134R)_eYFP, $10^{12}$ GC, 100 nl/min, Gene Vector and Virus Core at Stanford University, catalog #36) was delivered to the injection sites.

**Optogenetics experiments**

ChR2-expressing mPFC axons to MD thalamus neurons were activated using blue LEDs stimulations (Thorlabs M450LP2, 450 nm, duration 1 ms, maximal light intensity 13 mW, 19 mW/cm2) or blue lasers (Laserglow Technologies, 473 nm, duration 1 ms, maximal light intensity 8 mW, 10.8 mW/cm2). The mPFC-MD thalamus synaptic connection was evaluated using 10 light stimulations at both 1Hz and 10Hz, with one train administered every 20 seconds, while maintaining voltage clamp at -70mV. The resultant synaptic responses were evaluated in voltage clamp to measure synaptic current and in current clamp to quantify the number of action potentials. Synaptic properties parameters were measured using custom MATLAB code.

To investigate the receptor composition underlying the abnormal persistent current observed in adult Shank3$^{-/-}$ mutant mice, either DL-2-Amino-5-phosphonovaleric acid (AP5, Sigma, A5282) at a concentration of 100 µM (broad-spectrum NMDA receptor blocker) or (RS)-3,5-Dihydroxyphenylglycine (DHPG, Tocris, #0342) at a concentration of 10 µM (selective group I mGluR agonist) were applied for

10 minutes in the bath after obtaining a stable baseline recording. Partial washout was obtained in some cases. The impact of AP5 and DHPG on the 10Hz voltage-clamp synaptic response was quantified and compared to the baseline recordings. Statistical analysis, 2-way ANOVA with repeated measure, was performed to evaluate the significance of the effects observed.


## Acknowledgments

We thank all past and current lab members for their feedback during the project. We thank Katlin Villar, Cameron Glick and Nicole Agranonik for their help in managing mouse lines, laboratory equipment and supplies.

## Funding sources

This work was supported by SFARI award # 633450, Screening for convergence of axonal dysfunction across diverse mouse models of autism.


## References


1. Wetherby, A. M. *et al.* Early Indicators of Autism Spectrum Disorders in the Second Year of Life. *J Autism Dev Disord* **34**, 473–493 (2004).
2. De Giacomo, A. & Fombonne, E. Parental recognition of developmental abnormalities in autism. *European Child & Adolescent Psychiatry* **7**, 131–136 (1998).
3. Hodel, A. S. Rapid infant prefrontal cortex development and sensitivity to early environmental experience. *Developmental Review* **48**, 113–144 (2018).
4. Lai, J. K. Y. *et al.* Temporal and spectral differences in the ultrasonic vocalizations of fragile X knock out mice during postnatal development. *Behav Brain Res* **259**, 119–130 (2014).
5. Wang, X. *et al.* Altered mGluR5-Homer scaffolds and corticostriatal connectivity in a Shank3 complete knockout model of autism. *Nat Commun* **7**, 11459 (2016).
6. Klune, C. B., Jin, B. & DeNardo, L. A. Linking mPFC circuit maturation to the developmental regulation of emotional memory and cognitive flexibility. *eLife* **10**, e64567 (2021).
7. Kolk, S. M. & Rakic, P. Development of prefrontal cortex. *Neuropsychopharmacol.* **47**, 41–57 (2022).

552 8. Ferguson, B. R. & Gao, W.-J. Development of thalamocortical connections between the
553 mediodorsal thalamus and the prefrontal cortex and its implication in cognition. *Front.*
554 *Hum. Neurosci.* **8**, (2015).
555 9. Amodio, D. M. & Frith, C. D. Meeting of minds: the medial frontal cortex and social
556 cognition. *Nat Rev Neurosci* **7**, 268–277 (2006).
557 10. Yizhar, O. *et al.* Neocortical excitation/inhibition balance in information processing and
558 social dysfunction. *Nature* **477**, 171–178 (2011).
559 11. Lee, E. *et al.* Enhanced Neuronal Activity in the Medial Prefrontal Cortex during Social
560 Approach Behavior. *J. Neurosci.* **36**, 6926–6936 (2016).
561 12. Brumback, A. C. *et al.* Identifying specific prefrontal neurons that contribute to autism-
562 associated abnormalities in physiology and social behavior. *Mol Psychiatry* **23**, 2078–
563 2089 (2018).
564 13. Verpelli, C. *et al.* Importance of Shank3 protein in regulating metabotropic glutamate
565 receptor 5 (mGluR5) expression and signaling at synapses. *J Biol Chem* **286**, 34839–34850
566 (2011).
567 14. Moessner, R. *et al.* Contribution of SHANK3 mutations to autism spectrum disorder. *Am J*
568 *Hum Genet* **81**, 1289–1297 (2007).
569 15. Boccuto, L. *et al.* Prevalence of SHANK3 variants in patients with different subtypes of
570 autism spectrum disorders. *Eur J Hum Genet* **21**, 310–316 (2013).
571 16. Waga, C. *et al.* Identification of two novel *Shank3* transcripts in the developing mouse
572 neocortex. *J. Neurochem.* **128**, 280–293 (2014).
573 17. Rios, O. & Villalobos, J. Postnatal development of the afferent projections from the
574 dorsomedial thalamic nucleus to the frontal cortex in mice. *Developmental Brain*
575 *Research* **150**, 47–50 (2004).

18. Caruso, A., Marconi, M. A., Scattoni, M. L. & Ricceri, L. Ultrasonic vocalizations in laboratory mice: strain, age, and sex differences. *Genes Brain Behav* **21**, e12815 (2022).
19. Kalinowska, M. *et al.* Deletion of Fmr1 in parvalbumin-expressing neurons results in dysregulated translation and selective behavioral deficits associated with fragile X syndrome. *Molecular Autism* **13**, 29 (2022).
20. Jang, W. E. *et al.* Cntnap2-dependent molecular networks in autism spectrum disorder revealed through an integrative multi-omics analysis. *Mol Psychiatry* **28**, 810–821 (2023).
21. Tripathi, M. K. *et al.* Mutations associated with autism lead to similar synaptic and behavioral alterations in both sexes of male and female mouse brain. *Sci Rep* **14**, 10 (2024).
22. Liang, B. *et al.* Distinct and Dynamic ON and OFF Neural Ensembles in the Prefrontal Cortex Code Social Exploration. *Neuron* **100**, 700-714.e9 (2018).
23. Nicholson, C. & Freeman, J. A. Theory of current source-density analysis and determination of conductivity tensor for anuran cerebellum. *J Neurophysiol* **38**, 356–368 (1975).
24. Kumar, S. S. & Huguenard, J. R. Properties of Excitatory Synaptic Connections Mediated by the Corpus Callosum in the Developing Rat Neocortex. *Journal of Neurophysiology* **86**, 2973–2985 (2001).
25. Douglas, R. J., Koch, C., Mahowald, M., Martin, K. A. C. & Suarez, H. H. Recurrent Excitation in Neocortical Circuits. *Science* **269**, 981–985 (1995).
26. Kisvárday, Z. F. *et al.* Synaptic targets of HRP-filled layer III pyramidal cells in the cat striate cortex. *Exp Brain Res* **64**, 541–552 (1986).

27. Sacai, H. *et al.* Autism spectrum disorder-like behavior caused by reduced excitatory synaptic transmission in pyramidal neurons of mouse prefrontal cortex. *Nat Commun* **11**, 5140 (2020).

28. Anastasiades, P. G. & Carter, A. G. Circuit organization of the rodent medial prefrontal cortex. *Trends in Neurosciences* **44**, 550–563 (2021).

29. Ferguson, B. R. & Gao, W.-J. Thalamic Control of Cognition and Social Behavior Via Regulation of Gamma-Aminobutyric Acidergic Signaling and Excitation/Inhibition Balance in the Medial Prefrontal Cortex. *Biological Psychiatry* **83**, 657–669 (2018).

30. Ko, J. Neuroanatomical Substrates of Rodent Social Behavior: The Medial Prefrontal Cortex and Its Projection Patterns. *Front. Neural Circuits* **11**, (2017).

31. Testa-Silva, G. *et al.* Hyperconnectivity and Slow Synapses during Early Development of Medial Prefrontal Cortex in a Mouse Model for Mental Retardation and Autism. *Cerebral Cortex* **22**, 1333–1342 (2012).

32. Pirone, A. *et al.* Social Stimulus Causes Aberrant Activation of the Medial Prefrontal Cortex in a Mouse Model With Autism-Like Behaviors. *Front Synaptic Neurosci* **10**, 35 (2018).

33. Lee, A. T. *et al.* Pyramidal Neurons in Prefrontal Cortex Receive Subtype-Specific Forms of Excitation and Inhibition. *Neuron* **81**, 61–68 (2014).

34. Ramaswamy, S. & Markram, H. Anatomy and physiology of the thick-tufted layer 5 pyramidal neuron. *Front Cell Neurosci* **9**, 233 (2015).

35. McCormick, D. A. & Huguenard, J. R. A model of the electrophysiological properties of thalamocortical relay neurons. *Journal of Neurophysiology* (1992) doi:10.1152/jn.1992.68.4.1384.

621 36. McCormick, D. A. & Pape, H. C. Properties of a hyperpolarization-activated cation current
622 and its role in rhythmic oscillation in thalamic relay neurones. *The Journal of Physiology*
623 **431**, 291–318 (1990).
624 37. Rubenstein, J. L. R. & Merzenich, M. M. Model of autism: increased ratio of
625 excitation/inhibition in key neural systems. *Genes Brain Behav* **2**, 255–267 (2003).
626 38. Peixoto, R. T., Wang, W., Croney, D. M., Kozorovitskiy, Y. & Sabatini, B. L. Early
627 hyperactivity and precocious maturation of corticostriatal circuits in Shank3B−/− mice.
628 *Nat Neurosci* **19**, 716–724 (2016).
629 39. Peixoto, R. T. *et al.* Abnormal Striatal Development Underlies the Early Onset of
630 Behavioral Deficits in Shank3B Mice. *Cell Reports* **29**, 2016-2027.e4 (2019).
631 40. Luo, Y.-F. *et al.* Divergent projections of the prelimbic cortex mediate autism- and anxiety-
632 like behaviors. *Mol Psychiatry* **28**, 2343–2354 (2023).
633 41. Lazaro, M. T. *et al.* Reduced Prefrontal Synaptic Connectivity and Disturbed Oscillatory
634 Population Dynamics in the CNTNAP2 Model of Autism. *Cell Reports* **27**, 2567-2578.e6
635 (2019).
636 42. Kalmbach, B. E., Johnston, D. & Brager, D. H. Cell-Type Specific Channelopathies in the
637 Prefrontal Cortex of the fmr1-/y Mouse Model of Fragile X Syndrome. *eNeuro* **2**, (2015).
638 43. Brill, J. & Huguenard, J. R. Sequential changes in AMPA receptor targeting in the
639 developing neocortical excitatory circuit. *J Neurosci* **28**, 13918–13928 (2008).
640 44. Kroon, T., van Hugte, E., van Linge, L., Mansvelder, H. D. & Meredith, R. M. Early postnatal
641 development of pyramidal neurons across layers of the mouse medial prefrontal cortex.
642 *Sci Rep* **9**, 5037 (2019).
643 45. Durand, C. M. *et al.* Mutations in the gene encoding the synaptic scaffolding protein
644 SHANK3 are associated with autism spectrum disorders. *Nat Genet* **39**, 25–27 (2007).

46. Ha, H. T. T. *et al.* Shank and Zinc Mediate an AMPA Receptor Subunit Switch in Developing Neurons. *Front. Mol. Neurosci.* **11**, (2018).

47. Gogolla, N. *et al.* Common circuit defect of excitatory-inhibitory balance in mouse models of autism. *J Neurodevelop Disord* **1**, 172–181 (2009).

48. Antoine, M. W., Langberg, T., Schnepel, P. & Feldman, D. E. Increased Excitation-Inhibition Ratio Stabilizes Synapse and Circuit Excitability in Four Autism Mouse Models. *Neuron* **101**, 648-661.e4 (2019).

49. Guo, B. *et al.* Restoring thalamocortical circuit dysfunction by correcting HCN channelopathy in Shank3 mutant mice. *CR Med* **5**, (2024).

50. Marmolejo, N., Paez, J., Levitt, J. B. & Jones, L. B. Early postnatal lesion of the medial dorsal nucleus leads to loss of dendrites and spines in adult prefrontal cortex. *Dev Neurosci* **34**, 463–476 (2012).

51. Qin, L., Ma, K. & Yan, Z. Chemogenetic Activation of Prefrontal Cortex in Shank3-Deficient Mice Ameliorates Social Deficits, NMDAR Hypofunction, and Sgk2 Downregulation. *iScience* **17**, 24–35 (2019).

52. Benoit, L. J. *et al.* Adolescent thalamic inhibition leads to long-lasting impairments in prefrontal cortex function. *Nat Neurosci* **25**, 714–725 (2022).

53. Selimbeyoglu, A. *et al.* Modulation of prefrontal cortex excitation/inhibition balance rescues social behavior in *CNTNAP2* -deficient mice. *Sci. Transl. Med.* **9**, eaah6733 (2017).

54. Wang, W. *et al.* Chemogenetic Activation of Prefrontal Cortex Rescues Synaptic and Behavioral Deficits in a Mouse Model of 16p11.2 Deletion Syndrome. *J Neurosci* **38**, 5939–5948 (2018).

55. Ultrasonic Vocalizations in Rat and Mouse Pups - Hofer - 2001 - Current Protocols in Neuroscience - Wiley Online Library.

https://currentprotocols.onlinelibrary.wiley.com/doi/abs/10.1002/0471142301.ns0814s17.

56. Pennington, Z. T. *et al.* ezTrack: An open-source video analysis pipeline for the investigation of animal behavior. *Sci Rep* **9**, 19979 (2019).
57. Goto, T. *et al.* An evaluation of the conductivity profile in the somatosensory barrel cortex of Wistar rats. *J Neurophysiol* **104**, 3388–3412 (2010).
58. Arshadi, C., Günther, U., Eddison, M., Harrington, K. I. S. & Ferreira, T. A. SNT: a unifying toolbox for quantification of neuronal anatomy. *Nat Methods* **18**, 374–377 (2021).
59. Vantomme, G. *et al.* A Thalamic Reticular Circuit for Head Direction Cell Tuning and Spatial Navigation. *Cell Rep* **31**, 107747 (2020).

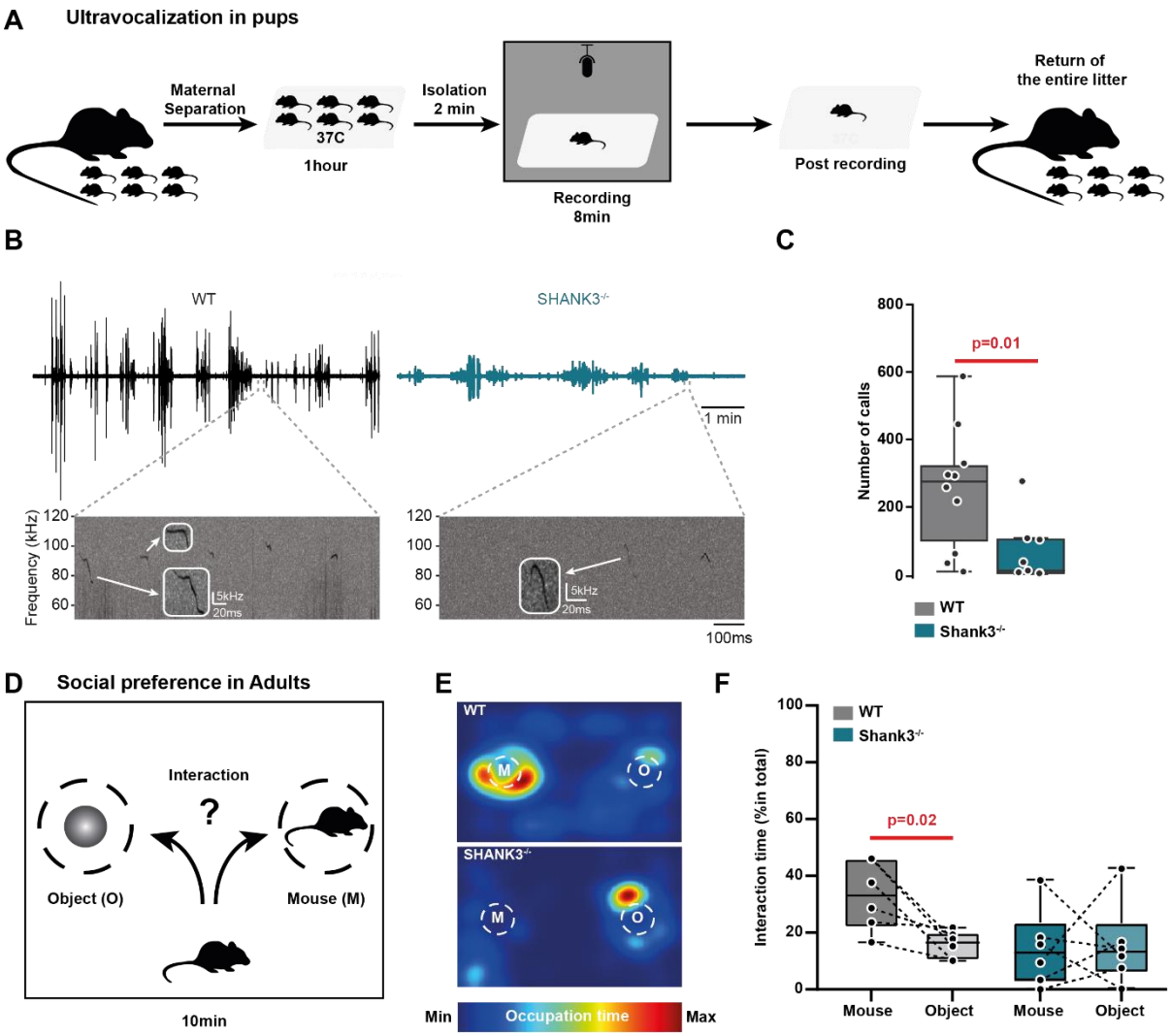


**Figure1. Shank3$^{-/-}$ mice display communication deficits in early life and social behavior deficits in adulthood.** (A) Schematic diagram of isolation and ultrasonic vocalization protocol performed in Shank3 WT and Shank3$^{-/-}$ P11 littermates. (B) Examples 8 minutes raw audio data (top traces) and 1 second filtered spectrogram (bottom images, in kHz) that display syllables. Insert in white represent a zoom on examples of individual syllable. Left: WT (black); Right (blue): Shank3. (C) Number of calls identified using Avisoft-SASLab Pro software for WT (grey) and Shank3$^{-/-}$ (blue). (D) Schematic diagram of social preference test performed in WT and Shank3$^{-/-}$ adults. (E) Example of occupation time heat maps for WT (top) and Shank3$^{-/-}$ (bottom) adults. (F) Percentage of the interaction time with a never-met conspecific (darker colors) or a novel inanimate object (lighter colors) for WT (grey) and Shank3$^{-/-}$ (blue).

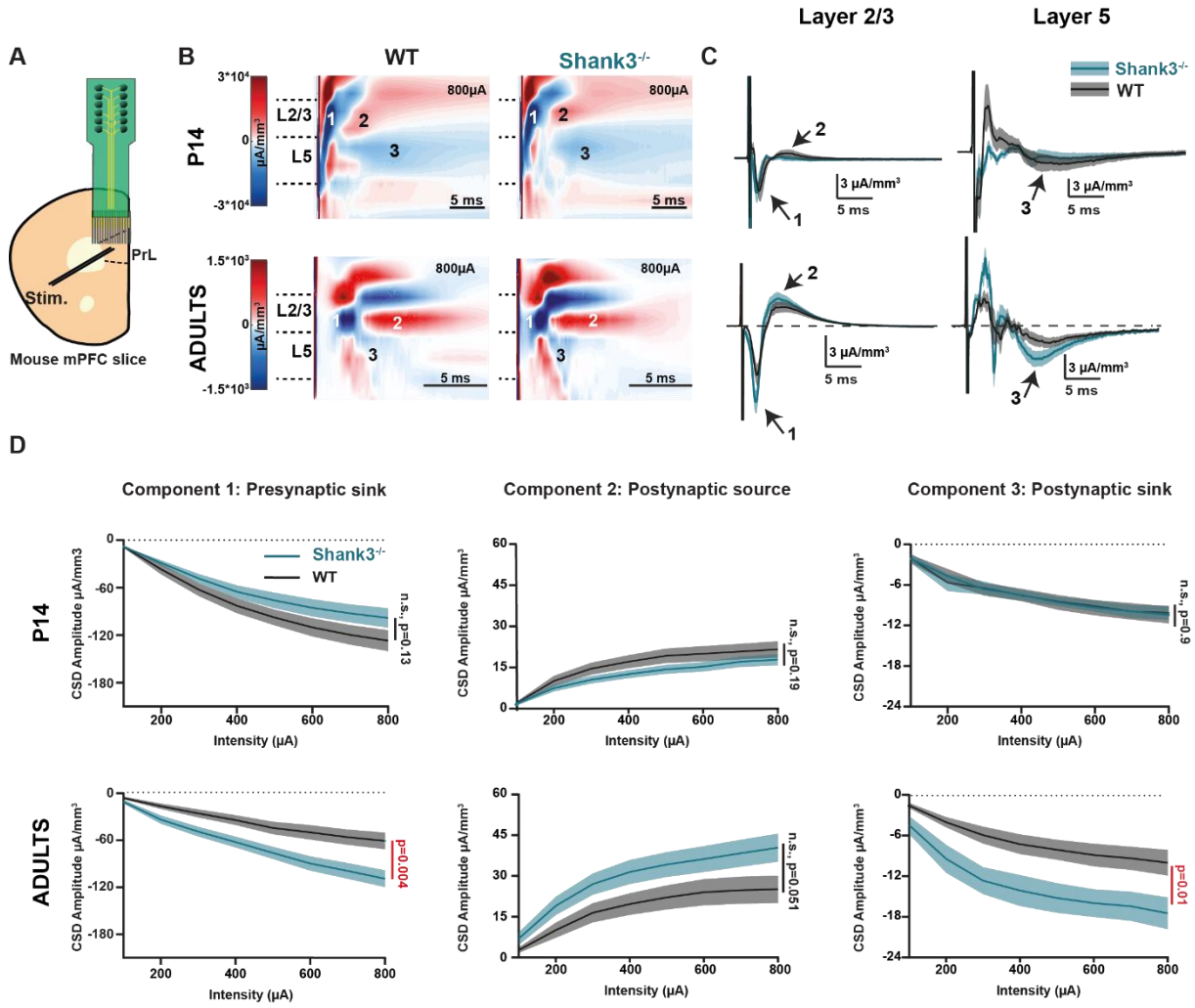


**Figure 2. Shank3$^{-/-}$ displays mPFC hyperfunction during adulthood but not during early life.** (A) Schematic of LFP recording across all mPFC layers while electrical stimulation is delivered in deep layers. (B) Average heatmap current source density (CSD) response of mPFC network during an 800µA stimulation in WT (left) and Shank3$^{-/-}$ (right) at P14 (top row; WT= 3 mice, 10 slices; Shank3$^{-/-}$ = 3 mice, 11 slices) and adults ( >P55, bottom row; WT= 5 mice, 12 slices; Shank3$^{-/-}$= 5 mice, 13 slices). (C) Average CSD response of the L2/3 presynaptic sink (arrow 1) and L2/3 postsynaptic source (arrow 2) and L5 postsynaptic sink (arrow 3) with maximal (800µA) stimulation with P14 (top row; WT (grey) = 3 mice, 10 slices; Shank3$^{-/-}$ (blue) = 3 mice, 11 slices) and adult slices ( >P55, bottom row; WT (grey) = 5 mice, 12 slices; Shank3$^{-/-}$ (blue) = 5 mice, 13 slices). Traces represent mean (solid line) ± sem (shaded line). (D) Input/ Output curve of CSD peak amplitude with stimuli ranging from 100 to 800 µA for P14 (top row) and adults (bottom row) WT (grey) and Shank3$^{-/-}$ (blue).

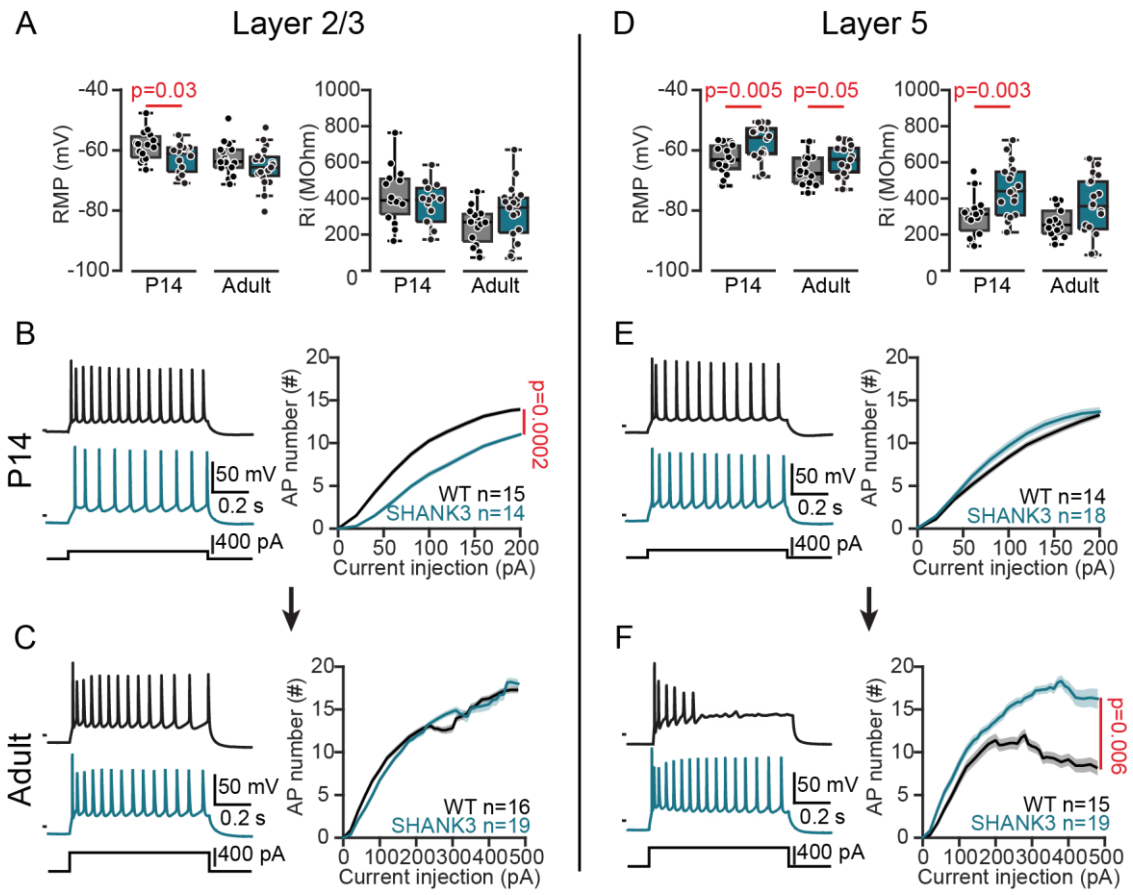


**Figure 3. Shank3$^{-/-}$ mice display early electrophysiological hypoexcitability in mPFC upper cortical layers to be replaced by hyperexcitability in deep layers in adulthood.**

(A) Resting membrane potential (RMP, left) and input resistance (Rm, right) of layer 2/3 pyramidal neurons from P14 and adult WT (grey) and Shank3$^{-/-}$ (blue) mice. (B) Left, representative action potential firing traces of layer 2/3 mPFC pyramidal cells at P14. Right, layer 2/3 pyramidal cells number of AP in response to current injection at P14. Traces represent mean ± sem. (C) Same as (B) in adult mice. (D) Resting membrane potential (RMP, left) and input resistance (Rm, right) of layer 5 pyramidal neurons from P14 and adult WT (grey) and Shank3$^{-/-}$ (blue) mice. (E) Left, representative action potential firing traces of layer 5 mPFC pyramidal cells at P14. Right, layer 5 pyramidal cells number of AP in response to current injection at P14. Traces represent mean ± SEM. (F) Same as (E) in adult mice.

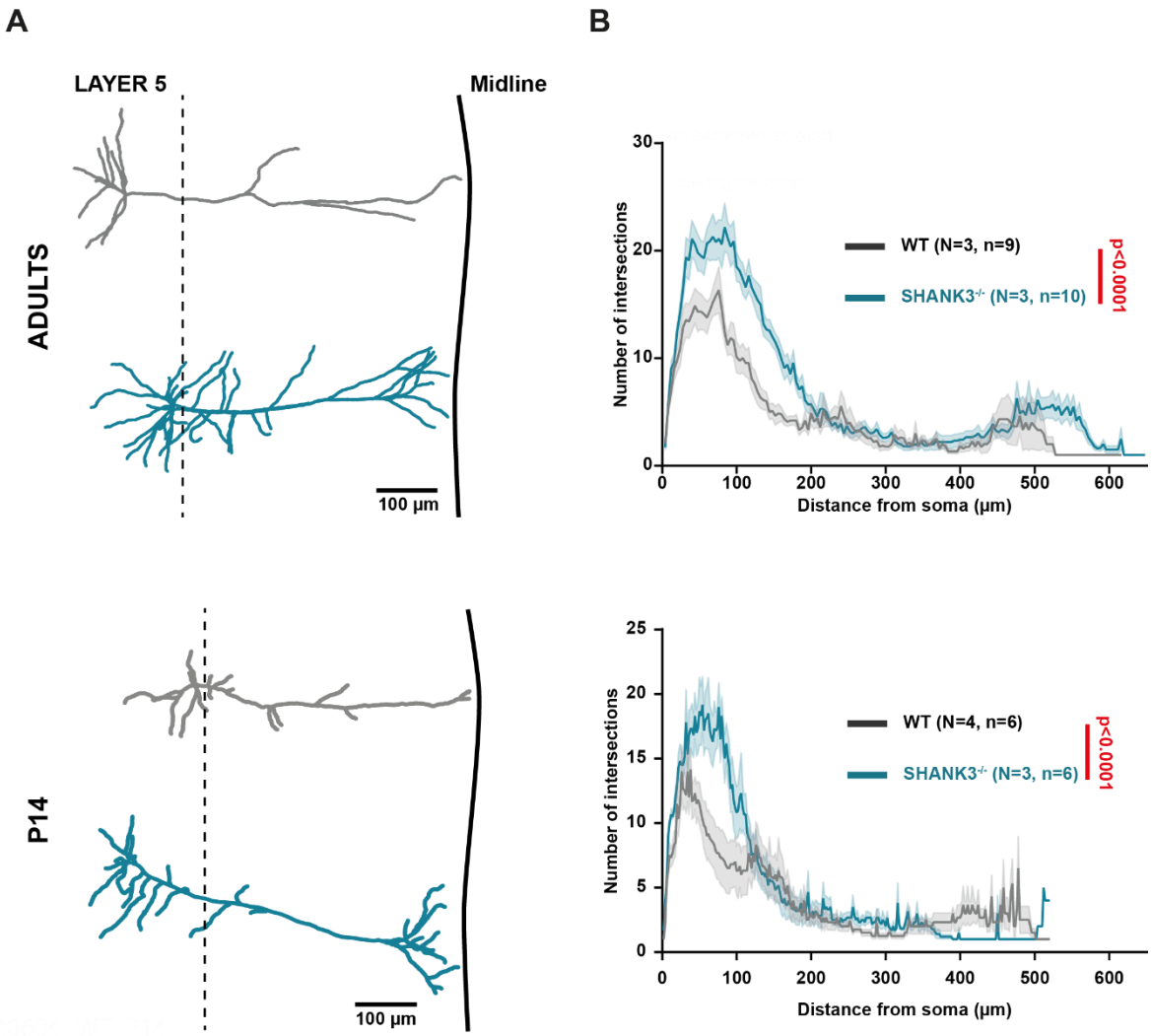


**Figure 4. mPFC layer 5 pyramidal neurons display increased dendritic complexity in Shank3$^{-/-}$ mice both in early life and in adulthood.** (A) Representative examples of mPFC layer 5 pyramidal cells of P14 (top) and adult (bottom) WT (grey) and Shank3$^{-/-}$ (blue) mice reconstructed using biocytin filling after patch-clamp. (B) Average Scholl analysis of mPFC layer 5 pyramidal cells of P14 (top) and adult (bottom) WT (grey) and Shank3$^{-/-}$ (blue) adult mice. Traces are represented as mean ± sem.

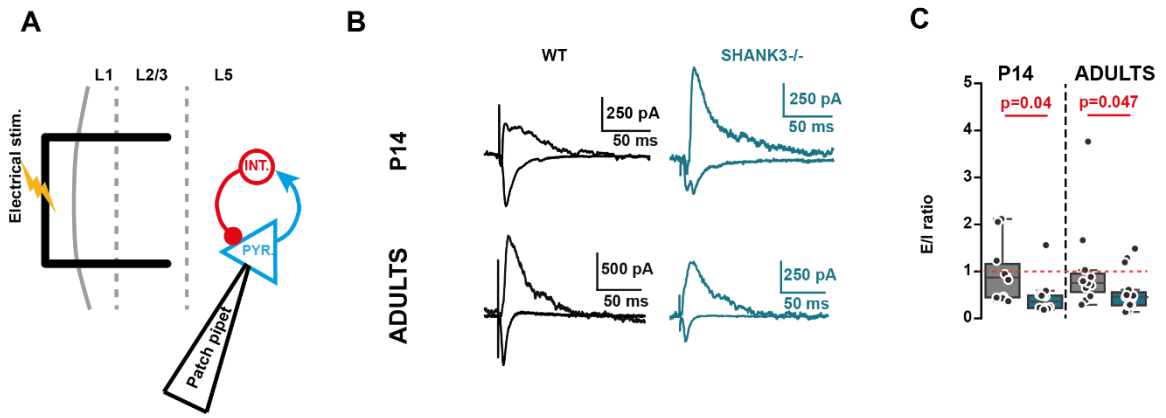


735

736 **Figure 5. Excitatory/inhibitory synaptic currents ratio is reduced in Shank3$^{-/-}$ mPFC L5 pyramidal**
737 **cells at both P14 and in adults.** (A) Experimental design to measure EPSCs (at -70mV) and IPSCs (at
738 +10mV) in mPFC slices. (B) Representative Excitatory - Inhibitory (E/I) current traces elicited in mPFC
739 layer 5 pyramidal cells by an electrical stimulation in layer 2/3 of P14 (top) and adult (bottom) WT (grey)
740 and Shank3$^{-/-}$ (blue) mice. (C) E/I ratio at P14 (left panel; WT (grey), 4 mice, 10 cells; Shank3$^{-/-}$ (blue),
741 5 mice, 12 cells) and adulthood (right panel; WT (grey), 7 mice, 11 cells; Shank3$^{-/-}$ (blue), 7 mice, 15
742 cells).

743

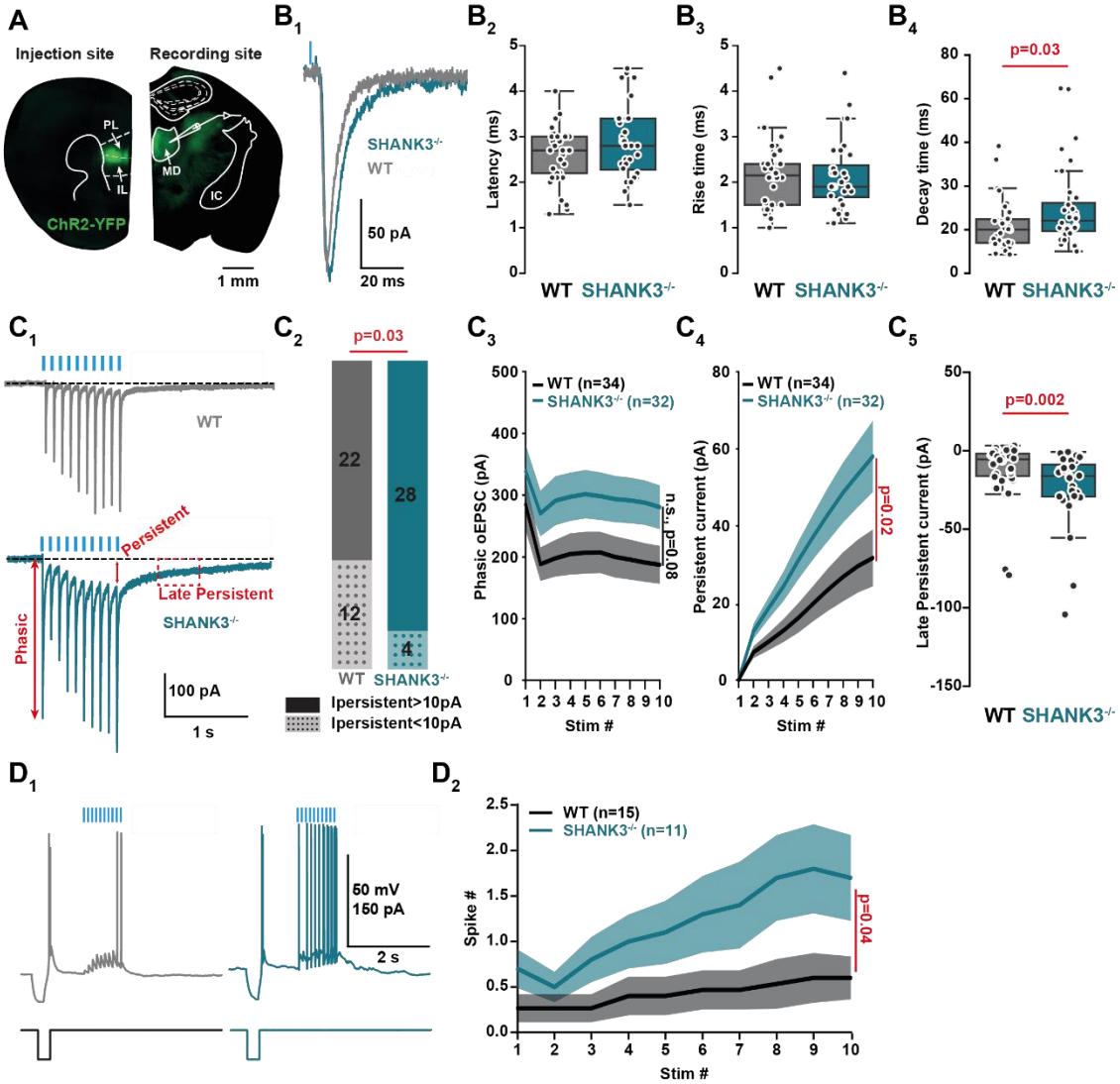


**Figure 6. Enhanced mPFC-MD synaptic function in adult Shank3$^{-/-}$ mice.** (A) Epifluorescence image of the injection site of AAV1_ChR2_YFP in mPFC (left) and labeled projections in MD thalamus (right). (B1) Representative optogenetically-evoked EPSC (oEPSC) from MD neurons from WT (grey) and Shank3$^{-/-}$ (blue) mice. (B2-B4) oEPSC latency rise time. and decay timefrom adult WT (grey, 16 mice, 34 cells) and Shank3$^{-/-}$ (blue, 12 mice, 32 cells). (C1) Representative oEPSC trains elicited with 10Hz stimulation. Phasic, persistent and late persistent current measurements are indicated in red. (C2) Proportions of cells with detectable (>10pA) or undetectable (<10pA) $I_{persistent}$ in MD cells of WT (grey) and Shank3$^{-/-}$ (blue) mice. (C3) Averaged phasic current amplitude with a 10Hz stimulation for WT (grey) and Shank3$^{-/-}$ (blue) mice. (C4) Averaged persistent current with a 10Hz stimulation for WT (grey) and Shank3$^{-/-}$ (blue) mice. (C5) Late persistent current for WT (grey) and Shank3$^{-/-}$ (blue) mice. (D1) Representative traces of current-clamp recordings of MD cells upon repeated activation of mPFC axons. (D2) Number of evoked action potentials during oEPSC trains from WT (black) and Shank3$^{-/-}$ (blue) mice. Traces represent mean±sem.

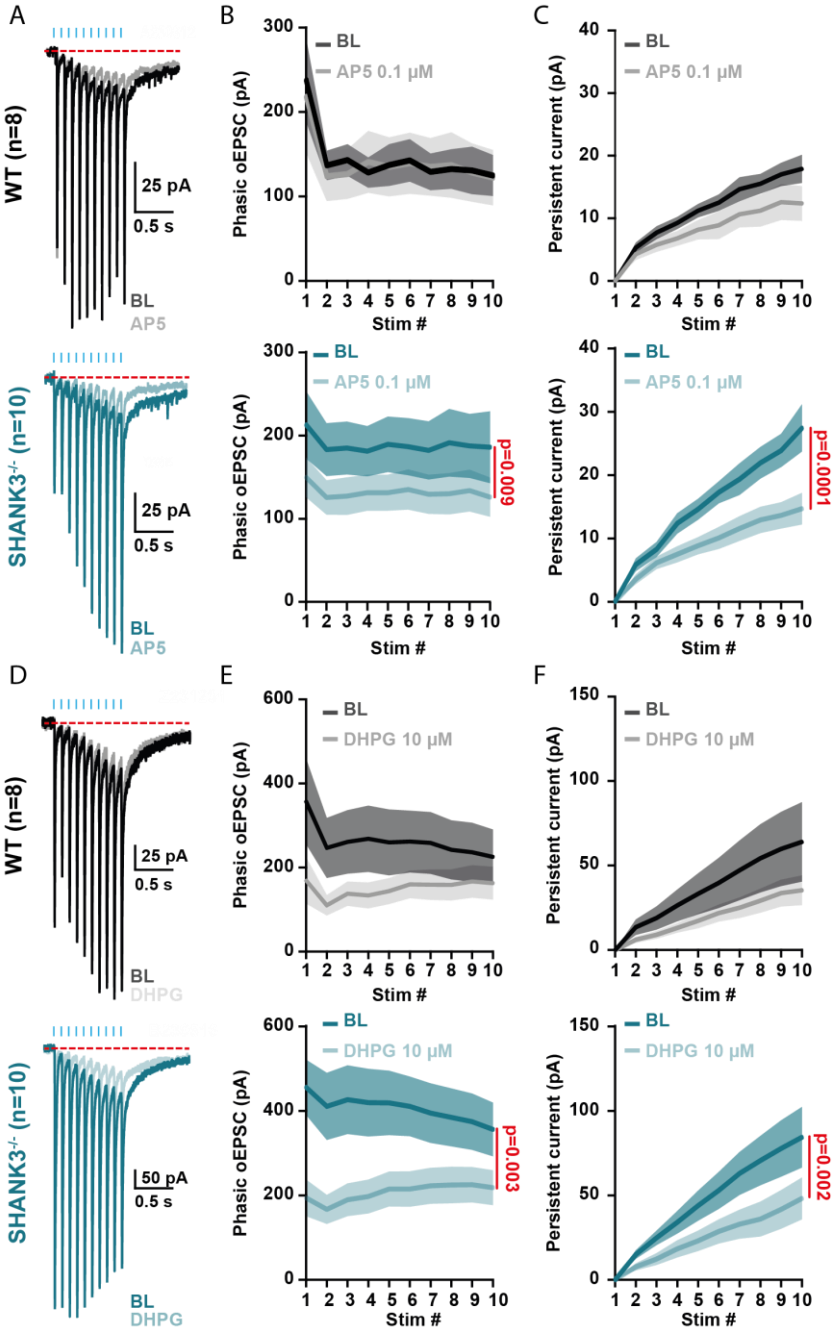


**Figure 7. mGluR and NMDARs contribution to the phasic and persistent MD oEPSC from mPFC activation in adult Shank3$^{-/-}$ mice.** (A) Representative oEPSCs elicited with 10Hz stimulation in MD before (dark color) and after 0.1uM AP5 (light color) for WT (grey, 6 mice, 8 cells) and Shank3$^{-/-}$ (blue, 3 mice, 10 cells) mice. (B) Phasic currents at 10Hz stimulation for WT (top, grey) and Shank3$^{-/-}$ (bottom, blue) mice before (BL, baseline, dark color) and during AP5 bath application (AP5 0.1uM, light color). (C) Same as (B) for persistent current. (D) Representative oEPSCs elicited with 10Hz stimulation in MD before (dark color) and after 10uM DHPG (light color) for MD recordings from WT (grey, 3 mice, 8 cells) and Shank3$^{-/-}$ (blue, 4 mice, 12 cells) mice. (E) MD phasic current with 10Hz stimulation for WT (top, grey) and Shank3$^{-/-}$ (bottom, blue) mice before (BL, baseline, dark color) and during AP5 bath application (AP5 0.1uM, light color). (F) Same as (E) for persistent current. Traces are represented are mean (solid line) ± sem (shaded line).